Brain aging shows nonlinear transitions, suggesting a midlife "critical window" for metabolic intervention

Botond B. Antal[a,b,c], Helena van Nieuwenhuizen[b,c,d], Anthony G. Chesebro[a,b,c], Helmut H. Strey[a,b,c], David T. Jones[e] (ID), Kieran Clarke[f], Corey Weistuch[g], Eva-Maria Ratai[c], Ken A. Dill[b,1] (ID), and Lilianne R. Mujica-Parodi[a,b,c,d,h,1] (ID)

Affiliations are included on p. 9.

Understanding the key drivers of brain aging is essential for effective prevention and treatment of neurodegenerative diseases. Here, we integrate human brain and physiological data to investigate underlying mechanisms. Functional MRI analyses across four large datasets (totaling 19,300 participants) show that brain networks not only destabilize throughout the lifetime but do so along a nonlinear trajectory, with consistent temporal "landmarks" of brain aging starting in midlife (40s). Comparison of metabolic, vascular, and inflammatory biomarkers implicate dysregulated glucose homeostasis as the driver mechanism for these transitions. Correlation between the brain's regionally heterogeneous patterns of aging and gene expression further supports these findings, selectively implicating GLUT4 (insulin-dependent glucose transporter) and APOE (lipid transport protein). Notably, MCT2 (a neuronal, but not glial, ketone transporter) emerges as a potential counteracting factor by facilitating neurons' energy uptake independently of insulin. Consistent with these results, an interventional study of 101 participants shows that ketones exhibit robust effects in restabilizing brain networks, maximized from ages 40 to 60, suggesting a midlife "critical window" for early metabolic intervention.

brain | aging | insulin | neuron | fMRI

Brain aging is associated with multiple degenerative processes, including glucose hypometabolism, atrophy, cerebrovascular disease, and deposition of beta-amyloid and tau proteins (1–5). However, these manifestations often become detectable only in the later stages of aging, beyond the point where effective intervention may be possible. In contrast, age-related neurological changes identified by functional MRI (fMRI) and electroencephalography (EEG) can be detected decades earlier (6, 7). Therefore, neuroimaging-based biomarkers hold the potential to identify mechanisms and evaluate treatments even during the prodrome, particularly if they are sensitive enough to measure response to intervention on short timescales.

Our previous research indicates that, at ages starting in the late 40s, both fMRI and EEG-derived brain networks (a whole-brain measure of neural connectivity, or signaling) undergo substantial reorganization, which can be characterized by destabilization and desynchronization (8–11). This reorganization is similar to that observed in individuals with Type 2 diabetes mellitus (T2DM), suggesting neuronal insulin resistance as a candidate mechanism driving early stages of brain hypometabolism and cognitive decline (1, 12). Mechanistically, we further showed that experimentally inducing neuronal insulin resistance by blocking GLUT4, the insulin-dependent glucose transporter (13–16), results in altered firing dynamics and slowed axonal conduction velocity, thus disrupting neuronal signaling (17). Finally, using multiscale computational modeling, we identified mechanistic pathways by which reduced ATP availability in neurons can lead to diminished potassium gradients, reduced axonal conduction velocity, and thus desynchronization of brain networks at the whole brain scale (11, 18).

While glucose is the brain's primary fuel, ketones provide an alternative that can be metabolized by neurons without insulin and thus can bypass insulin resistance. Because this alternative fuel can be utilized by insulin-resistant neurons, ketones have been proposed as a potential therapeutic for age-related hypometabolism (19–22). Ketones, whether produced endogenously through fasting or low-carbohydrate/high-fat diets or administered exogenously as a supplement, have been shown to improve age-related cognitive decline (23–25) and to restore insulin-resistance-induced deficits in axonal conduction velocity (17). Moreover, ketones may improve neural functioning even at

Significance

Age-related cognitive decline is associated with metabolic, vascular, and inflammatory changes, making it challenging to distinguish primary causes from secondary (downstream) effects. This study demonstrates that brain aging follows a specific progression, with the first stage occurring in middle age and coinciding with increased insulin resistance. Moreover, we show that brain areas that age fastest are also those most vulnerable to neuronal insulin resistance. Importantly, we find that administering ketones, which can fuel neurons while bypassing insulin resistance, reverses brain aging effects. However, this intervention is only effective when provided early enough for neurons to remain viable. These findings contribute to our understanding of brain aging mechanisms and suggest neurometabolic strategies for targeted early intervention in preventing age-related cognitive decline.

baseline, strengthening signaling for neurons without being compromised by insulin resistance (17) and across the brain for younger individuals in their 20s and 30s (8, 9). This increased metabolic efficiency under ketosis is consistent with effects reported for other organs, such as the heart (24, 26–28).

Here, we integrate our lifespan brain-aging trajectory, mechanistic, and interventional findings, with a specific focus on distinguishing earlier catalyzing processes from later downstream effects. First, we established the robustness of the nonlinear (sigmoid) trajectory identified by our prior findings (8) by testing the replication of brain network destabilization curves across four independent large-scale fMRI datasets totaling 19,300 subjects. Second, once the brain aging trajectory was confirmed, we asked which physiological changes co-occurred with its nonlinear transition points: the sigmoid's base α, and its inflection point I. Third, we asked which mechanistic factors were implicated by the spatially heterogeneous nature of brain aging. Identifying which brain regions were differentially affected earlier than others, we compared age-related spatial heterogeneity with that of gene expression to ask which mechanisms were consistent with or excluded by the aging pattern. Both physiological biomarker and gene expression analyses confirmed neuronal insulin resistance as the driving mechanism for the brain aging trajectory. Based on these results, we then extended the ketone intervention beyond the aging trajectory's baseline (ages 20 to 39 y) (8) to investigate the impact of ketosis on 101 subjects' brains following the onset α of network destabilization (the metabolic stress period, ages 40 to 59 y) and its inflection I (ages 60 to 79 y). As with our prior studies, ketones were fasting-normalized, individually weight-dosed, and calorically matched with glucose to isolate their differential effects with greater precision than possible with dietary studies of ketosis. Our results indicate the beneficial effects are maximized during the period of most rapid network destabilization, during ages 40 to 59 y. This suggests a critical window for intervention: a period of neuronal metabolic stress, preceded by homeostasis and followed by hypometabolism, during which the regulatory mechanisms that maintain the brain's optimal energy supply "bend" before they "break."

Results

Metabolic Changes Predominate during the Acceleration Phase of Brain Aging, as Depicted by Nonlinear Lifespan Trends in Brain Network Instability. Using four large-scale neuroimaging datasets (HCP-A, UK Biobank [UKB], Mayo Clinic Study of Aging, and Cam-CAN), we first reproduced our previously measured nonlinear trends in brain network instability (*SI Appendix,* Fig. S1), focusing on the three subnetworks that were identified as most sensitive to aging: auditory, visual, and cingulo-opercular (*SI Appendix,* Fig. S2) (8). However, the neuroimaging field lacks a neurobiological or methodological consensus regarding the many ways one can parse and categorize resting-state subnetworks (29–35). Therefore, to maximize generalizability, we also extended network instability analyses to encompass all-to-all (whole-brain) networks. We then maximized detection sensitivity by focusing on those datasets with the highest (<1 s) temporal resolution (36–40): HCP-A and UKB. In both datasets, whole-brain networks exhibited a significant destabilization across the lifespan (linear fit, HCP-A: t = 8.25, $P < 1E-10$, N = 712; UKB dataset: t = 3.8, $P = 0.0002$, N = 16,435).

To quantify the observed nonlinear trajectory, we fitted a sigmoid model to the data, which, for HCP-A, provided a significantly better fit as compared to the linear trend (F-test, F = 1.5, $P = 1E-8$) (Fig. 1A). From the parameters of the sigmoid model, we identified three key transition points, or landmarks: $\alpha = 43.7$ y, marking the onset of destabilization; $I = 66.7$ y, marking the age of most rapid destabilization (the sigmoid's inflection point); and $\beta_1 = 89.7$ y, marking the age at which destabilization has reached its plateau. For UKB, the sigmoid model yielded a superior fit as compared to the null model (F = 5.0, $P < 1E-10$); however, unlike HCP-A, UKB did not show a significant improvement as compared to the linear model (F = 0.29, $P = 1$). This is likely due to UKB's narrower age range, whose lower bounds coincided with the start of the destabilization period (*SI Appendix,* Fig. S3). From the fitted sigmoid parameters from the UKB dataset, the derived age landmarks were $\alpha = 46.9$ y, $I = 61.5$ y, and $\beta_1 = 76.1$ y. We confirmed that head motion was not a confounding variable (r = −0.02, $P = 0.7$) (*SI Appendix,* Fig. S4).
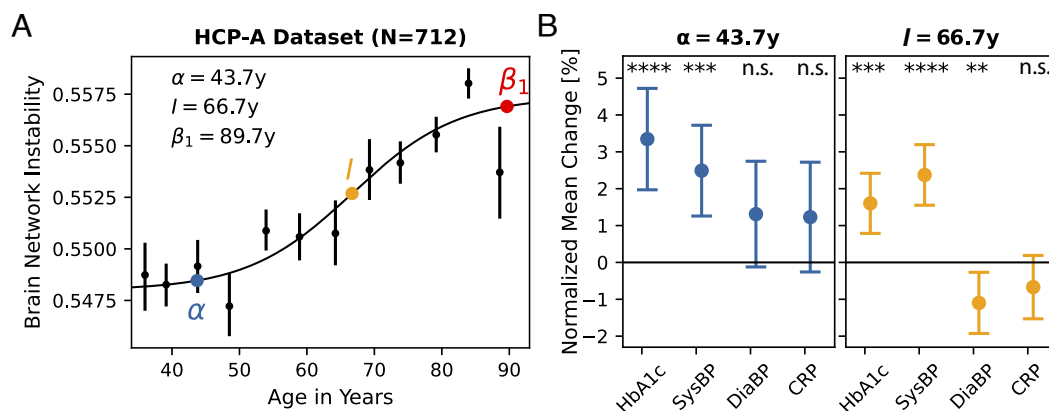

Fig. 1. Metabolic changes predominate during the acceleration phase of brain aging, as depicted by nonlinear lifespan trends in brain network instability. (A) The HCP-A functional neuroimaging dataset revealed a sigmoidal trend in the destabilization of brain networks across the lifespan. Curve fitting was utilized to derive landmark age points α (onset of destabilization), I (age of fastest destabilization), and β_1 (age of destabilization plateau). (B) Mean changes for biomarkers representing metabolic health (HbA1c), vascular health [systolic blood pressure (SysBP), diastolic blood pressure (DiaBP)], and inflammatory state [blood levels of C-reactive protein (CRP)] were evaluated across age groups defined with respect to their relationship to the α and I landmarks ($N_{age<\alpha} = 111$, $N_{\alpha \leq age < I} = 281$, $N_{I \leq age < \beta_1} = 202$). Error bars represent 95% CIs for the mean changes between consecutive age groups, normalized by the variance of each biomarker across the entire age range. The α landmark was associated most strongly with an increase in HbA1c (t = 4.8, $P = 4E-6$), while the I landmark was associated most strongly with an increase in systolic blood pressure (t = 5.7, $P = 3E-8$). In contrast, blood CRP, indicative of inflammation, showed no significant changes around either landmark. n.s., not statistically significant, *$P \leq 0.05$; **$P \leq 0.01$; ***$P \leq 0.001$; ****$P \leq 0.00001$.

Table 1. Summary of utilized neuroimaging datasets

Dataset	Sample size (female)	Age range (median)	Field strength (fMRI)	Acquisition length	Repetition time
HCP-A	712 (396)	36 to 90 (58)	3T	25 min 30 s	0.8 s
UKB	16,435 (8,374)	50 to 80 (64)	3T	6 min	0.735 s
Metabolic	101 (48)	21 to 79 (44)	7T	9 min 53 s	0.802 s
Mayo Clinic	1,519 (692)	31 to 90 (70)	3T	7 min 50 s	2.925 s
Cam-CAN	634 (320)	18 to 88 (54)	3T	8 min 40 s	1.97 s

HCP-A: Human Connectome Project Aging Dataset, UKB: UK Biobank, Metabolic: Metabolic intervention dataset collected at Massachusetts General Hospital, Mayo: Mayo Clinic Study of Aging Dataset, Cam-CAN: Cambridge Centre for Ageing and Neuroscience Dataset.

To investigate driving mechanisms underlying the observed destabilization, we further narrowed down our analyses to focus on the HCP-A dataset, due to its broader age range and inclusion of biomarkers specific to each of three candidate mechanisms: metabolic (blood HbA1c), vascular (systolic and diastolic blood pressure), and inflammatory (blood c-reactive protein). These measures were then used to identify whether any significant physiological changes coincided with the inferred landmark points. We divided the sample into subgroups bounded by the age landmark points ($N_{age<\alpha} = 111$, $N_{A\leq age<I} = 281$, $N_{I\leq age<\beta_1} = 202$), with the group older than $\beta_1 = 89.7$ y omitted due to small sample size. Two-sample t tests revealed the α landmark to be associated most consistently with a marked increase in HbA1c ($t = 4.8$, $P = 4E-6$), accompanied by less consistent elevations in systolic blood pressure ($t = 4.0$, $P = 0.0001$) (Fig. 1B). In contrast, the I landmark was most consistently associated with profound vascular changes, with systolic blood pressure displaying the greatest effect size ($t = 5.7$, $P = 3E-8$), followed by HbA1c ($t = 3.9$, $P = 0.0001$) and then diastolic blood pressure ($t = 2.6$, $P = 0.01$) (Fig. 1B). Notably, no significant changes were detected in blood C-reactive protein levels around either landmark. These findings suggest that changes in energy metabolism predominate at the onset of brain network destabilization, while alterations in vascular biomarkers become evident only later, during the rapid phase of destabilization.

Gene Expression Brain Maps Highlight Neuronal Insulin Resistance as a Driver of Brain Aging, Counteracted by Neuronal Ketone Transport. To further understand how each of the candidate mechanisms relates to the sigmoidal lifespan trajectory, we considered the spatial heterogeneity of brain aging and its correspondence to patterns of regional gene expression (Fig. 2A). To identify age-related changes in brain activity, we first measured each brain's amplitude of low-frequency fluctuations (ALFF), a voxel-based measure of brain activity (41) (ALFF was normalized for each individual brain; thus, ALFF provided a measure of relative, rather than absolute, activity across the brain). Using these ALFF values, we then computed age-specific brain activity maps, which were subsequently compared to mechanistic gene expression maps provided by the Allen Human Brain Atlas (42, 43). To compute spatial similarity, we corrected for spatial autocorrelations and multiple comparisons. We first interpreted the genes that significantly correlated with aging effects in an unsupervised manner using gene set enrichment analysis (44). This analysis highlighted pathways associated with synaptic function and transmembrane transport (*SI Appendix*, Fig. S7). Next, based on our lifespan findings suggesting metabolic dysregulation as a potential driver mechanism, we tested six genes encoding for glucose transporters (GLUT1, GLUT3, GLUT4), ketone/lactate transporters (MCT1, MCT2), and APOE. As control variables, we analyzed matched sets of

six genes each, representing vascular processes, inflammation, and a set of genes with no known association to any of the three candidate mechanisms (Table 2). Among these 24 genes, only three, all metabolism-related, exhibited significant correlations with aging patterns in both the UKB and HCP-A datasets (Fig. 2B). In contrast, the control genes associated with vascular function, inflammation, and otherwise unrelated mechanisms did not show replicable correlations across both datasets (*SI Appendix*, Fig. S8), suggesting that the observed patterns of functional brain aging were specific to energy metabolic processes.

Three metabolic genes were significantly correlated ($\alpha = 0.05$, Bonferroni corrected) with age-related changes in brain activity. These were the neuronal insulin-dependent glucose transporter GLUT4 (UKB: $r = 0.28$, $P = 0.0003$; HCP-A: $r = 0.3$, $P = 0.0007$), the neuronal lactate/ketone transporter MCT2 (UKB: $r = -0.37$, $P = 0.00003$; HCP-A: $r = -0.35$, $P = 0.002$), and the lipid transporter APOE (UKB: $r = 0.35$, $P = 0.0003$; HCP-A: $r = 0.34$, $P = 0.001$), whose $\epsilon 4$ allele markedly increases risk for Alzheimer's disease (Fig. 2C) (45–47). The absence of significant correlations with glial (astrocyte) glucose and ketone/lactate transporters GLUT1 and MCT1, as well as the neuronal insulin-independent glucose transporter GLUT3, further isolate mechanisms specific to neuron, insulin, and lipid-related metabolism. The inverse correlation with MCT2 suggests these aging effects may be potentially mitigated by neuronal lactate/ketone transport.

D-β-Hydroxybutyrate Circumvents Insulin Resistance to Reverse Brain Network Destabilization during the Accelerated Phase of Brain Aging. The gene expression results reported above not only show that brain aging effects are consistent with compromised GLUT4 but also identify ketone uptake through MCT2 as a potential mitigating pathway (Fig. 3A). Using ultrahigh field (7T) fMRI, we previously showed that acute administration of individually weight-dosed exogenous ketone monoester (hereafter referred to as D-β-hydroxybutyrate [D-βHB], its hydrolysis product), but not calorically matched glucose, stabilizes brain networks in premidlife adults (<50 y) (8). Here, we conduct the same within-subjects protocol (Metabolic Intervention Study; Fig. 3B), but extend it to include α (ages 40 to 59 y) and I (60 to 79 y) transition points along the brain aging trajectory (Table 1). To normalize for test–retest variance between each participant's D-βHB and glucose testing days ($r = 0.44$, *SI Appendix*, Fig. S5), all network stability values were individually baseline-corrected to their own prebolus fasting values on that day.

Our fMRI results indicated that, for the 20- to 39-y-old age group (pre-α), D-βHB significantly stabilized brain networks compared to fasting ($t = -2.6$, $P = 0.01$, $N = 38$). For the 40- to 59-y-old age group (post-α), the effect size of ketone monoester was 84.62% larger than that of the youngest group
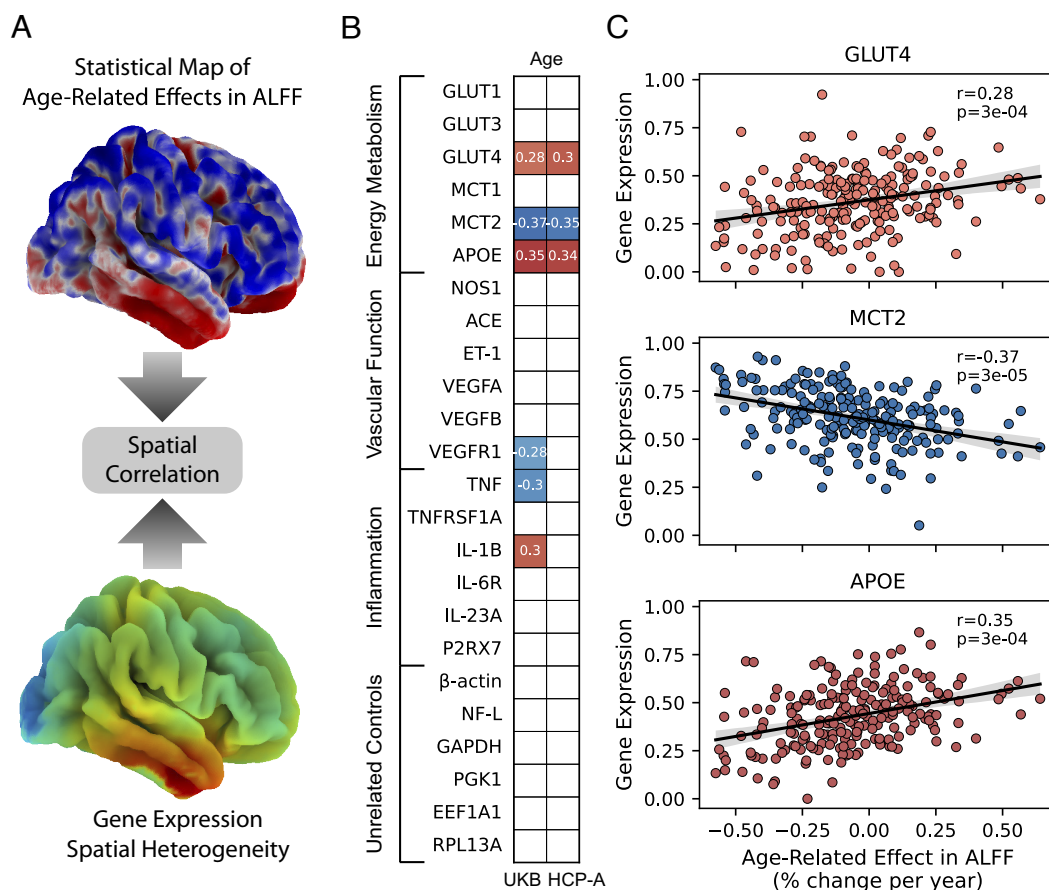
Fig. 2. Gene expression brain maps highlight neuronal insulin resistance as a driver of brain aging, counteracted by neuronal ketone transport. (*A*) Diagram illustrating the methodology for establishing similarity between the aging pattern in brain function and gene expression distribution. (*B*) Color-coded tiles show Spearman correlations between the pattern of age-related changes in ALFF and the spatial distribution of gene expression associated with probable key mechanisms underlying brain aging. Each shown point corresponds to a cortical functional region of interest. Labels indicate expressed proteins rather than the underlying genes. Investigated mechanisms encompassed cellular glucose uptake (genes translated to GLUT1, GLUT3, GLUT4), ketone/lactate uptake (MCT1, MCT2), lipid-transport (APOE), vascular function (NOS1, ACE, ET-1, VEGFA, VEGFB, VEGFR1), inflammation (TNF, TNF receptor 1, IL-1β, IL-6, IL-23A, P2RX7), and housekeeping and cytoskeletal structure as unrelated controls (ACTB, NF-L, GAPDH, PGK1, EEF1A1, RPL13A). The spatial correlations were computed in both UKB and HCP-A datasets. (*C*) Scatter plots depict associations between brain aging effects and gene expression (log-scaled) for genes that replicated in both the UKB and HCP-A datasets. These included genes encoding for GLUT4, MCT2, and APOE. The functional data shown are from the UKB dataset.

(t = −4.8, P = 0.00003, N = 39). In contrast, for the 60- to 79-y-old age group (*I*), the effect size of ketone monoester was less than half that of the youngest group (t = −0.8, P = 0.4, N = 24) (Fig. 3*C*). Meanwhile, in agreement with our previous results in young adults, the glucose bolus calorically matched to each participant's D-βHB dose did not show stabilizing effects in any of the age groups (Fig. 3*C*), indicating that the results were specific to non-GLUT4 (and thus noninsulin) mediated pathways.

Finally, we checked for evidence of potential confounding factors that might explain the age-related effects of the intervention (critical window) in ways unrelated to energy utilization. Head Motion: We previously established in the HCP-A dataset that head motion did not correlate with brain network instability (r = −0.02, P = 0.7) (*SI Appendix*, Fig. S4). For the Metabolic Intervention Study dataset, we likewise confirmed that changes in motion did not correlate with the observed effects (r = 0.09, P = 0.4) (*SI Appendix*, Fig. S6) and, therefore, could not explain the markedly diminished effect size in the oldest age group. Variance: Bartlett's test indicated no significant difference between the variances of the 40- to 59-y-old and 60- to 79-y-old age groups (B = 1.0, P = 0.3), suggesting that the absence of significant findings in the oldest group was due to a smaller

mean effect rather than increased variance. Ketone Dosing: Mean blood ketone levels following D-βHB administration were 3.9±1.1 mmol/L, reflecting a high physiological concentration, and did not differ between the 40- to 59-y-old and 60- to 79-y-old age groups (t = −1.3, P = 0.2). Blood–Brain Barrier: Finally, to test whether reduced effects in the oldest subjects might reflect changes in D-βHB's ability to cross the blood–brain barrier, we scanned a representative subset (N = 41) of our Intervention Study cohort with 7T proton (1H) magnetic resonance spectroscopy (MRS). Our results confirmed a lack of significant age-related differences, either absolute or relative, in D-βHB within the brain (*SI Appendix*, Fig. S9). Thus, our MRS results suggest that age-related changes in efficacy result not from differences in the concentration of ketones within the brain but rather from the degree to which the ketones can be metabolized.

Discussion

In biological systems, "stress" occurs when the control mechanisms that maintain homeostasis are challenged by deviations beyond physiologically optimal ranges. While biological systems typically use negative feedback to compensate for small

Table 2. List of genes with expression maps investigated for spatial associations with aging effects

Gene	Protein product	Full name	Function	Mechanism group
SLC2A1	GLUT1	Glucose Transporter 1	Astrocytic and endothelial glucose transporter	Energy Metabolism
SLC2A3	GLUT3	Glucose Transporter 3	Neuronal insulin-independent glucose transporter	Energy Metabolism
SLC2A4	GLUT4	Glucose Transporter 4	Neuronal insulin-dependent glucose transporter	Energy Metabolism
SLC16A1	MCT1	Monocarboxylate Transporter 1	Astrocytic lactate and ketone transporter	Energy Metabolism
SLC16A7	MCT2	Monocarboxylate Transporter 2	Neuronal lactate and ketone transporter	Energy Metabolism
APOE	APOE	Apolipoprotein E	Cholesterol transporter	Energy Metabolism
NOS1	NOS1	Nitric Oxide Synthase 1	Catalyst for nitric oxide synthesis	Vascular Function
ACE	ACE	Angiotensin-Converting Enzyme	Vasoconstriction regulator	Vascular Function
EDN1	ET-1	Endothelin 1	Vasoconstrictor	Vascular Function
VEGFA	VEGFA	Vascular Endothelial Growth Factor A	Vascular growth regulator	Vascular Function
VEGFB	VEGFB	Vascular Endothelial Growth Factor B	Vascular growth regulator	Vascular Function
FLT1	VEGFR1	Vascular Endothelial Growth Factor Receptor 1	VEGF receptor	Vascular Function
TNF	TNF	Tumor Necrosis Factor	Proinflammatory cytokine	Inflammation
TNFRSF1A	TNFRSF1A	Tumor Necrosis Factor Receptor Superfamily Member 1A	TNF receptor	Inflammation
IL1B	IL-1β	Interleukin-1 Beta	Proinflammatory cytokine	Inflammation
IL6R	IL-6R	Interleukin-6 Receptor	IL-6 receptor	Inflammation
IL23A	IL-23A	Interleukin-23 Subunit Alpha	Proinflammatory cytokine	Inflammation
P2RX7	P2RX7	P2X Purinoceptor 7	Regulator of inflammatory signaling	Inflammation
ACTB	ACTB	Beta-Actin	Cytoskeletal protein	Unrelated Control
NEFL	NF-L	Neurofilament Light Polypeptide	Cytoskeletal protein	Unrelated Control
GAPDH	GAPDH	Glyceraldehyde 3-phosphate Dehydrogenase	Housekeeping glycolytic enzyme	Unrelated Control
PGK1	PGK1	Phosphoglycerate Kinase 1	Housekeeping glycolytic enzyme	Unrelated Control
EEF1A1	EEF1A1	Eukaryotic Translation Elongation Factor 1 Alpha 1	Protein synthesis elongation factor	Unrelated Control
RPL13A	RPL13A	Ribosomal Protein L13a	Ribosomal assembly factor	Unrelated Control

perturbations, more profound changes in the cellular milieu that exceed the capacity of the control system to compensate will eventually break the system. Insulin resistance is a perturbation that directly impacts cells by impairing GLUT4-mediated utilization of glucose (48). With glucose as brain cells' primary fuel source, insulin resistance, therefore, induces hypometabolism, a state of metabolic stress. We previously showed, using pharmacologically induced neuronal insulin resistance with neuronal field recordings, that metabolic stress slows axonal conduction velocity, reversed when neurons are administered the same D-βHB provided to participants here in our Metabolic Intervention study (17). This would result in long-range desynchronization (18), consistent with the observed network destabilization with age and its reversal by D-βHB.

Within control systems physiology, the canonical trajectory of sigmoid and collapse (Fig. 3D) is consistent with a breakdown in homeostatic regulation, in which the system bends before it eventually breaks. Here, we show that the destabilization of fMRI-derived functional networks does not follow a linear pattern but instead exhibits distinct landmarks, with the earliest transition point, α, co-occurring with a significant increase in systemic insulin resistance, measured by HbA1c. Additionally, our gene expression analyses suggest that the primary effect is

neuronal (MCT2) rather than glial (GLUT1, MCT1) and that the effect is not only generally glucose hypometabolism but tied specifically to insulin-dependent (GLUT4) rather than insulin-independent (GLUT3) neuronal glucose transport. We further show that brain networks can be restored by D-βHB. This fuel bypasses insulin resistance, during a hypothesized critical window when neurons are already beginning to be metabolically stressed, but before sustained starvation causes them to be irreversibly damaged (breaking point and subsequent cell death). Although a recent positron emission tomography (PET) study showed that neurons in elderly individuals, including those with mild cognitive impairment and Alzheimer's disease (22), still demonstrate ketone uptake, the beginnings of irreversible pathological changes at this stage may limit their therapeutic impact. Consistent with this, we observed the effects of D-βHB to diminish markedly during the 60- to 79-y range. The observed landmarks of brain aging correspond with those identified using systemic multiomics markers of aging in other studies (49, 50), providing further links between molecular mechanisms and our neurobiological results. Behaviorally, the attenuation of the effects of D-βHB coincides with the age at which cognitive decline begins to accelerate (51, 52) and when clinical symptoms typically manifest (53). Importantly, all of our neuroimaging analyses
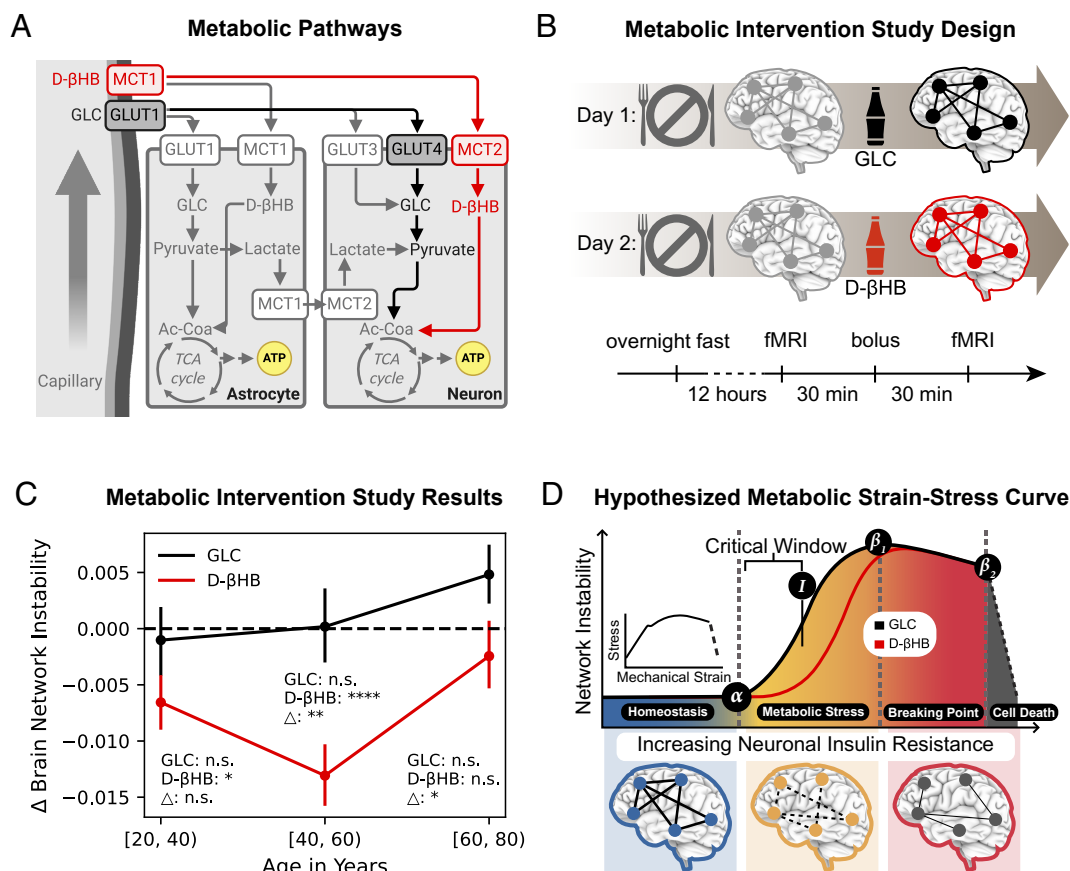
Fig. 3. D-*β*-hydroxybutyrate circumvents insulin resistance to reverse brain network destabilization during the accelerated phase of brain aging. (*A*) Oxidative energy-providing pathways of the brain. Neurons can utilize glucose, ketones, or lactate (via astrocytes) for energy, with distinct transporters facilitating their uptake. D-*β*HB is one of the primary ketones readily metabolized by neurons. The uptake of D-*β*HB, along with lactate, relies on insulin-signaling independent monocarboxylate transporters (MCT). Graphics were created with BioRender.com. (*B*) Experiment design of the metabolic intervention dataset. Each participant was scanned two separate times, time-locked to eliminate diurnal variability, with the D-*β*HB ketone monoester individually weight-dosed (395 mg/kg). Each individual's glucose dose was then calorie matched to their D-*β*HB ketone monoester dose. (*C*) Baseline (fasting) subtracted effects of the two metabolic interventions involving glucose and D-*β*HB ketone monoester on brain network instability. D-*β*HB stabilizes brain networks in age groups 20 to 39 ($P = 0.01$) and 40 to 59 ($P = 0.00003$) but not in 60 to 79 ($P = 0.4$). The administration of calorically matched glucose did not have significant effects. GLC: glucose vs. fasting, D-*β*HB: D-*β*HB vs. fasting, Δ: glucose vs. D-*β*HB. (*D*) Neuronal metabolism "bends" before it "breaks?" Nonlinear threshold effects of functional network destabilization, hypothesized to result from insulin resistance disruption of neuronal connectivity. n.s., not statistically significant, *$P \leq 0.05$; **$P \leq 0.01$; ***$P \leq 0.001$; ****$P \leq 0.00001$.

measured network stability at rest. Thus, one area for future investigation is whether, under cognitive load with higher energy demands, energy constraints may be evident at even younger ages (51, 54).

Mechanistically, the transition in neurons' functioning from "bending" to "breaking" can reflect various pathological changes before cell death, which become irreversible past critical thresholds. The formation of stable protein aggregates, such as tau and alpha-synuclein fibrils, can initiate self-perpetuating cycles of aggregation that persist even after the initial trigger is removed (55, 56). Mitochondrial DNA damage from oxidative stress often proves irreparable, leading to permanent compromise of cellular energy production (57). In the central nervous system, axonal degeneration beyond certain points becomes irreversible, particularly in the presence of inhibitory molecules and glial scarring (58). Some stress-induced epigenetic modifications become permanently "locked in," altering gene expression patterns and potentially maintaining inflammatory states (59). Additionally, advanced cellular senescence represents a point of no return, where neurons not only lose normal function but actively harm surrounding tissue through the senescence-associated secretory phenotype (60). However, many early pathological changes remain potentially reversible if identified and treated promptly,

emphasizing the critical importance of early intervention in neurological conditions.

One key conceptual challenge with devising a strategy for early intervention in brain aging is that the process involves many mutually interacting and reinforcing mechanisms. In particular, clinical studies of brain aging have implicated complex interactions between metabolic, immune, and vascular systems, suggesting interconnected cycles of dysregulation that can accelerate aging processes. For example, mitochondrial dysfunction can generate excessive reactive oxygen species that damage vascular endothelium and activate inflammatory pathways (61). This vascular damage is exacerbated by age-related reductions in cerebral blood flow, which compromise the delivery of nutrients and removal of metabolic waste products (62). The resulting tissue stress triggers microglial activation and promotes chronic low-grade inflammation or "inflammaging," characterized by elevated proinflammatory cytokines that further impair metabolic and vascular function (63). Blood–brain barrier dysfunction emerges as a critical nexus in this interaction, as it affects immune cell trafficking, metabolic substrate availability, and overall brain homeostasis (64). These changes are further complicated by cellular senescence, which affects all three systems through the senescence-associated secretory phenotype (SASP), promoting

sustained inflammation and tissue dysfunction (65). This intricate interplay creates self-reinforcing cycles where dysfunction in one system can propagate through the others, potentially accelerating cognitive decline and increasing susceptibility to age-related neurological diseases. Thus, from a treatment perspective, it is critical to determine whether brain aging, at its very earliest stages, represents a "perfect storm," in which many independent mechanisms all converge to dysregulate simultaneously, or whether there is a driving mechanism, the targeting of which might then mitigate the catalysis of other mechanisms.

Our mechanistic findings replicated across three complementary study designs, a strategy that reflects the need to compensate for some unavoidable limitations of each method. First, we analyzed a large-scale group sampled over the preclinical trajectory of brain aging, with the assumption that changes seen earlier in the aging process are more likely to be driving mechanisms, while changes seen later in the aging process are more likely to be downstream effects. While suggestive, one obvious caveat of this approach is that the minimally invasive and clinically ubiquitous physiological biomarkers most likely to be available in lifespan studies (e.g., HbA1c, BP, CRP) are not the most sensitive mechanistically. Therefore, the order in which we show those effects may reflect the sensitivity of the biomarkers more than the order, mechanistically, in which the damage occurs. For this reason, we provide additional confirmation of the physiological biomarker results by testing the relationship between patterns of brain activity and colocated gene expression. However, the interpretation of gene expression analyses also merits several important considerations. Given the challenges of quantifying gene expression in the human brain, we utilized microarray data from the open Allen Human Brain Atlas (42, 43), independent of the neuroimaging datasets used in our study. The Allen Atlas was derived from six adults, ages 24 to 57 y, without known neuropathology and presents averaged data, thereby missing differential changes in gene expression that may develop in later stages of aging. However, the baseline characteristics of this dataset capture predisposition, making it better suited for identifying driving mechanisms in the early stages of brain aging, which is the central focus of our work. With the complete dataset including 16,826 genes, we selected a targeted subset of drastically smaller size to allow highlighting individual genes and their correspondence to specific mechanisms. This level of detail is typically not achievable with unsupervised approaches, which yield large functional groups of pathways instead (*SI Appendix*, Fig. S7). Nevertheless, the gene set enrichment analysis, which highlighted synaptic processes, can be considered consistent with our supervised analysis. Given that synapses are the primary sites of activity-dependent neuronal GLUT4 translocation (66), genes with expression correlating with synaptic density are likely to appear indirectly implicated through this relationship. It is important to note, that while gene expression levels are closely related to the abundance of their corresponding protein products, significant deviations can occur within the same tissue due to posttranscriptional and posttranslational mechanisms (67–69). Future efforts that systematically assess these deviations or provide more direct measures of the human brain's proteome could enhance the mechanistic insights gained through these analyses. Further supporting the physiological biomarker and gene expression results, we demonstrated that an acute intervention that bypasses neuronal insulin resistance was able to reverse the aging effects. In this case, the fact that ketosis was induced within minutes was key in isolating mechanisms. Nutritional ketosis is known to systemically affect all three candidate mechanisms: metabolic, immune (70), and

vascular (71, 72). However, we have previously shown that the acute intervention, at the timescales measured in our study (30 to 60 min postbolus), affects neuronal signaling (17), and thus neuronal connectivity (18) and network stability (11), but not biomarkers for neuroinflammation such as myo-inositol (73), nor do they solely reflect hemodynamic changes that might confound fMRI (11). A final note relates to the specificity of neuronal insulin resistance as the driving mechanism for metabolic stress. While our results implicate metabolic changes as occurring prior to vascular and immune changes, it is also important to consider that neuronal insulin resistance may itself be caused by even earlier age-related changes in neuronal mitochondrial functioning (74, 75)—an important topic for future research.

Most neuroimaging research on dementia has been carried out on individuals presenting with the first signs and symptoms of the disease (76). However, the focus on an already-impaired population may not be the most strategic choice when probing disease etiology, for two reasons. First, by the time patients become symptomatic, the disease has progressed sufficiently so that it will be difficult to distinguish between pathophysiological features that are driving factors versus those that are secondary or interaction-based effects. Second, neurons that are metabolically stressed due to their inability to utilize glucose might still be capable of utilizing ketones as an alternate fuel source (77). If so, any attempt to restore or normalize neuronal function with ketones will only be feasible if the target neurons remain viable. Thus, for both scientific and clinical reasons, our primary focus here is the preclinical biomarkers during which neuronal metabolic stress can be detected, but before the onset of symptoms. By comparing neuro-energetics before, during, and after these presumptive biomarkers, we hope to provide a better understanding of the breakdown of underlying regulatory processes that drive nonlinear threshold effects in neurodegeneration and to use this understanding to identify the most strategic period for intervention. Our results motivate future larger-scale and longitudinal approaches, to test whether treatments targeting neuronal insulin resistance during the metabolic critical window can delay or prevent the onset of later brain changes, including glucose hypometabolism, atrophy, cerebrovascular disease, deposition of beta-amyloid and tau proteins, and cognitive decline.

Methods

Lifespan Neuroimaging Datasets. To investigate lifespan trends, we utilized resting-state fMRI data from four publicly available large neuroimaging datasets. These were the UK Biobank (UKB) (78), the Human Connectome Project Aging Lifespan 2.0 dataset (HCP-A) (79), Mayo Clinic study of Aging Dataset (80) and the Cambridge Centre for Ageing and Neuroscience (Cam-CAN) dataset (81). Corresponding characteristics are summarized in Table 1.

Metabolic Dataset. To investigate the impact of acute administration of D-βHB ketone monoester and calorically matched glucose on the stability of brain networks, resting-state fMRI data were collected from a cohort of healthy adults aged between 21 and 79 y (Table 1). This study was registered as a clinical trial on ClinicalTrials.gov (identifier NCT04106882) and was conducted under the oversight of the Institutional Review Board (IRB) at Massachusetts General Hospital (Boston, MA). Additionally, the IRB at State University of New York at Stony Brook (Stony Brook, NY) reviewed and approved the protocol to ensure compliance with institutional policies. Participants were recruited from the Boston metropolitan area through advertisements. Exclusion criteria included MRI contraindications, neurological or psychiatric disorders, history of brain injury, insulin resistance, diabetes mellitus, recreational drug usage, heavy alcohol usage, and recent adherence to low-carbohydrate diets. After

obtaining informed consent, participants underwent a physical examination and completed the Standardized Mini-Mental State Examination (SMMSE) to confirm cognitive normalcy. Subsequently, on a separate occasion following an overnight fast, participants underwent MRI scanning to establish a baseline, received either D-βHB ketone monoester or glucose, and went through another MRI scan 30 min postadministration, a time point previously identified to yield stable concentrations of both D-βHB and glucose in the brain (8). This procedure was replicated on a different day (time-locked), with participants being administered the alternate metabolite, thus establishing a within-subject experimental design. Both D-βHB ketone monoester and glucose were administered in liquid format in unlabeled containers. The D-βHB ketone monoester solution was prepared using pure (R)-3-hydroxybutyl-(R)-3-hydroxybutyrate monoester (ΔG ketone monoester, HVMN Inc., Miami, FL) dosed at 395 mg per kg of body weight and diluted with water (volume ratio 1:1.6). The glucose solution was a glucose tolerance test beverage in orange flavor (Fisher Scientific Inc., Pittsburg, PA), matched in caloric content to the D-βHB ketone monoester drink. We collected data from a total of 104 subjects. Three subjects were excluded from all analyses due to excessive motion, as indicated by a mean framewise displacement exceeding 0.5 mm during their scans. The subjects included in the analyses were balanced for sex within each of the three age groups (male/female, 20 to 39: 20/18, 40 to 59: 21/18, and 60 to 79: 12/12).

MRI Acquisition. The metabolic dataset was obtained using ultrahigh-field (7T) MRI, which included whole-brain blood oxygen level–dependent (BOLD) [echoplanar imaging (EPI)] and T1-weighted structural [multiecho magnetization prepared rapid gradient echo (MEMPRAGE)] images. BOLD images were captured using a quantitatively optimized protocol for detecting resting-state networks. This optimization process was performed using a dynamic phantom (BrainDancer; ALA Scientific Instruments) (82). The resulting protocol for BOLD acquisition included a simultaneous multislice (SMS) slice acceleration factor of 5, R = 2 acceleration in the primary phase encoding direction (48 reference lines), and online generalized autocalibrating partially parallel acquisition (GRAPPA) image reconstruction. Additional acquisition parameters comprised a repetition time (TR) of 802 ms, echo time (TE) of 20 ms, flip angle of 33°, voxel size of $2 \times 2 \times 1.5$ mm, with a total acquisition time of 9 min 53 s (740 volumes). T1-weighted structural volumes were acquired with 1 mm isotropic voxel size and four echoes using a protocol with TE1 = 1.61 ms, TE2 = 3.47 ms, TE3 = 5.33 ms, TE4 = 7.19 ms, TR = 2,530 ms, flip angle of 7.0°, R = 2 acceleration in the primary phase encoding direction (32 reference lines), and online GRAPPA image reconstruction, resulting in a total volume acquisition time of 6 min and 3 s. Information regarding 7T proton (1H) MRS methods can be found within the *SI Appendix*.

Image Preprocessing. UKB and HCP-A data were accessed in an already preprocessed format. Mayo, Cam-CAN, and the metabolic intervention datasets were preprocessed with fMRIprep (83), combined with image processing methods from SPM (SPM12, UCL) and the nilearn python library (84). The T1-weighted anatomical images were bias-field corrected first, then skull-stripped, and normalized to Montreal Neurological Institute (MNI) templates. BOLD contrast functional images obtained from each participant were realigned to account for head movement, slice-time corrected, and adjusted for geometric distortions caused by the magnetic field inhomogeneity. The latter step was carried out by coregistering the BOLD reference to the intensity-inverted T1-reference (85). These steps were followed by coregistration with the anatomical images and normalization to MNI space. Mean signals derived from white matter and cerebrospinal fluid voxels were regressed out from all time-series to mitigate physiological confounds, along with six motion regressors to minimize motion-related artifacts. Last, spatial smoothing with full width at half maximum of 5 mm was applied to the data before proceeding to further steps tailored to the specific metrics described later.

Brain Network Instability. Brain network instability is a scalar measure of the persistence of functional brain networks over time, which we utilized in prior work (8, 11). It quantifies the similarity between subsequent time windows (or snapshots) of functional connectivity across the entire time-series (*SI Appendix,*

Fig. S1). Larger values indicate more unstable brain networks. To compute brain network instability, the preprocessed data underwent additional processing steps. First, clean voxel-space BOLD time-series were band-pass filtered (0.04 to 0.1 Hz) where the high-pass filter was determined according to current guidelines in relation to the size of the time windows (86). Next, the filtered time-series were parceled into the Seitzman functional region of interest (ROI) atlas (87), which defines 13 functional subnetworks. Subsequently, the parceled time-series were then binned into nonoverlapping time windows, each with a length of 24 s. For each snapshot, all-to-all signed correlations were computed using the Ledoit–Wolf covariance estimator. Following this, difference matrices were computed between subsequent snapshots and then compressed into one scalar per snapshot pair using the L2 norm. Finally, averaging across every pair of snapshots yielded a single scalar per acquisition, representing brain network instability. In analyses focusing on specific subnetworks, these computations were limited to correlations exclusively between nodes within the corresponding subnetwork.

Sigmoid Curve Fitting. To characterize the nonlinear lifespan trend in brain network destabilization, we fitted a sigmoid function with four parameters to the dataset comprising age and brain network instability pairs:

$$y = y_{min} + \frac{R}{1 + \exp(-k \cdot (x - l))}. \quad [1]$$

The variables x and y represented age and brain network instability, respectively, while the four fitted parameters were defined as follows: y_{min}, denoting the minimum brain network instability; R, indicating the difference between the extremes; k, representing the rate of increase at the inflection point; and l, specifying the location of the inflection point. We utilized scipy.optimize (88). To ensure robust fitting, we conducted 20 independent optimization runs with different initializations and selected the best-fitting result. Subsequently, we conducted F-tests to evaluate the goodness of fit of the sigmoid function against both linear and null models. Additionally, we identified landmark age points along the sigmoid curve denoted as α and β_1, signifying the beginning and end of the nonlinear transition, respectively. These landmark points were quantified using the parameters derived from the fitted sigmoid function:

$$\alpha = l - log\left(\frac{0.95}{0.05}\right)/k \quad [2]$$

$$\beta_1 = l + log\left(\frac{0.95}{0.05}\right)/k. \quad [3]$$

Amplitude of Low-Frequency Fluctuations. The amplitude of low-frequency fluctuations (ALFF) is a metric utilized in resting-state fMRI analysis to assess regional spontaneous neuronal activity based on the BOLD signal (41). It involves quantifying the integrated power within a specific frequency range (usually 0.01 to 0.1 Hz), which corresponds to fluctuations originating from neuronal sources. In the temporal domain, this equates to the SD of the signal. We quantified ALFF in the HCP-A and UKB datasets. The cleaned and spatially smoothed voxel-space time-series were first band-pass filtered (0.01 to 0.1 Hz), and then the SD was computed from the resulting signals to yield ALFF for every voxel. Next, given the arbitrary scaling of the signal across different imaging sessions, we normalized each ALFF with the mean ALFF value calculated from all voxels within the brain mask for each subject individually. As a result, the subsequent quantification of age-associated effects represented relative reorganization rather than absolute increases or decreases across the lifespan. To quantify these age-related effects, we first parceled the computed ALFF values with the previously described Seitzman functional ROI atlas (87) to reduce computational costs. Next, we fitted linear regression models independently for each ROI with ALFF as the dependent variable and age as the independent variable (89). We then extracted the regression coefficient corresponding to age to quantify the effect size. Finally, for each ROI, we divided the computed effect size with the mean ALFF value across all subjects.

Spatial Correlations with Gene Expression. We utilized gene expression brain maps from the Allen Human Brain Atlas (42, 43), which represent log

values of mRNA expression at the voxel level across the brain. We initially filtered this dataset for genes included in brain-specific gene sets reported in ref. 90. This filtering process preserved 87% of the original 16,826 genes. Subsequently, we selected a subset of genes that encode proteins representative of three mechanistic groups: metabolic, vascular, and inflammatory mechanisms (Table 2). Next, we parceled the selected gene expression maps into the 300 ROIs to align them with the ALFF-derived statistical maps of age effects. We then filtered for cortical ROIs by selecting those regions overlapping with cortical structures outlined in the Automated Anatomical Labeling atlas (91). To quantify the similarity between the parceled gene expression maps and the fMRI statistical maps, we computed Spearman correlations while accounting for spatial autocorrelation in line with current standards. We utilized neuromaps (92) to generate spatial maps with similar autocorrelation structures. We generated 1,000 of these maps and computed Spearman correlations for each, resulting in a distribution of correlation values across all permutations. These resulting correlations were then combined and fitted with a normal distribution, from which we quantified the statistical significance of the Spearman correlation between the observed gene expression map and the statistical brain map from fMRI. Finally, to account for multiple comparisons, the resulting P-values were Bonferroni corrected.

Group Comparisons. We employed independent-sample t tests using scipy.stats (88) to compare biomarkers around the identified landmark points. To assess the effects of metabolic interventions on brain network instability, we conducted paired sample t-tests, enabled by the within-subject experiment design. Prior to all group comparisons, we removed statistical outliers using an interquartile range (IQR)–based method, where IQR is calculated as the absolute difference between the third quartile (Q3) and the first quartile (Q1). Data points exceeding 1.5 times the IQR above Q3 or below Q1 were discarded.

Data, Materials, and Software Availability. Data for this study were sourced from publicly available datasets, including the Human Connectome Project Aging Dataset, UK Biobank, Mayo Clinic Study of Aging Dataset, and Cambridge Centre for Ageing and Neuroscience Dataset. Additionally, we utilized an in-house metabolic dataset [Protecting the Aging Brain (PAgB) Dataset], which is accessible on openneuro.org via the following link: https://openneuro.org/datasets/ds005405 (93). The code used for data processing and analysis is available at https://www.lcneuro.org/analytic/networkstability (94).

Author affiliations: [a]Department of Biomedical Engineering, State University of New York at Stony Brook, Stony Brook, NY; [b]Laufer Center for Physical and Quantitative Biology, State University of New York at Stony Brook, Stony Brook, NY; [c]Athinoula A. Martinos Center for Biomedical Imaging, Massachusetts General Hospital, Harvard Medical School, Boston, MA; [d]Department of Physics, State University of New York at Stony Brook, Stony Brook, NY; [e]Department of Neurology, Mayo Clinic, Rochester, MN; [f]Department of Physiology, Anatomy, and Genetics, University of Oxford, Oxford United Kingdom; [g]Department of Medical Physics, Memorial Sloan Kettering Cancer Center, New York, NY; and [h]Santa Fe Institute, Santa Fe, NM

Author contributions: E.-M.R., K.A.D., and L.R.M.-P. designed research; B.B.A. and H.v.N. performed research, H.H.S and K.C. contributed new reagents/analytic tools; B.B.A., H.v.N., A.G.C., and C.W. analyzed data; H.H.S and D.T.J. facilitated access to the datasets; and B.B.A. and L.R.M.-P. wrote the paper.

Reviewers: P.C., University of Minnesota Twin Cities; and M.P.M., National Institute on Aging (NIH).

Competing interest statement: The intellectual property covering the manufacture and use of the ketone ester is owned by the University of Oxford and the NIH and is licensed to TdeltaS Global Inc. K.C., as an inventor, receives a share of the royalties under the terms prescribed by each institution. K.C. is a director of TdeltaS Ltd., a company spun out of the University of Oxford to develop products based on the science of ketone bodies in human nutrition.

1. S. M. De la Monte, J. R. Wands, Alzheimer's disease is type 3 diabetes-evidence reviewed. *J. Diabetes Sci. Technol.* **2**, 1101–1113 (2008).
2. L. Mosconi, Glucose metabolism in normal aging and Alzheimer's disease: Methodological and physiological considerations for pet studies. *Clin. Transl. Imaging* **1**, 217–233 (2013).
3. L. Pini *et al.*, Brain atrophy in Alzheimer's disease and aging. *Ageing Res. Rev.* **30**, 25–48 (2016).
4. M. P. Mattson, T. V. Arumugam, Hallmarks of brain aging: Adaptive and pathological modification by metabolic states. *Cell Metab.* **27**, 1176–1199 (2018).
5. M. A. DeTure, D. W. Dickson, The neuropathological diagnosis of Alzheimer's disease. *Mol. Neurodegener.* **14**, 32 (2019).
6. C. E. Wierenga, M. W. Bondi, Use of functional magnetic resonance imaging in the early identification of Alzheimer's disease. *Neuropsychol. Rev.* **17**, 127–143 (2007).
7. R. Sperling, The potential of functional MRI as a biomarker in early Alzheimer's disease. *Neurobiol. Aging* **32**, S37–S43 (2011).
8. L. R. Mujica-Parodi *et al.*, Diet modulates brain network stability, a biomarker for brain aging, in young adults. *Proc. Natl. Acad. Sci. U.S.A.* **117**, 6170–6177 (2020).
9. C. Weistuch *et al.*, Metabolism modulates network synchrony in the aging brain. *Proc. Natl. Acad. Sci. U.S.A.* **118**, e2025727118 (2021).
10. R. M. Razban, B. B. Antal, K. A. Dill, L. R. Mujica-Parodi, Brain signaling becomes less integrated and more segregated with age. *Network Neurosci.* **8**, 1051–1064 (2024).
11. H. van Nieuwenhuizen *et al.*, Ketosis regulates K^+ ion channels, strengthening brain-wide signaling disrupted by age. *Imaging Neurosci.* **2**, 1–14 (2024).
12. B. Antal *et al.*, Type 2 diabetes mellitus accelerates brain aging and cognitive decline: Complementary findings from UK biobank and meta-analyses. *eLife* **11**, e73138 (2022).
13. C. Leloup *et al.*, Discrete brain areas express the insulin-responsive glucose transporter GLUT4. *Brain Res. Mol. Brain Res.* **38**, 45–53 (1996).
14. S. El Messari *et al.*, Immunocytochemical localization of the insulin-responsive glucose transporter 4 (GLUT4) in the rat central nervous system. *J. Comp. Neurol.* **399**, 492–512 (1998).
15. S. El Messari, A. Ait-Ikhlef, D. H. Ambroise, L. Penicaud, M. Arluison, Expression of insulin-responsive glucose transporter GLUT4 mRNA in the rat brain and spinal cord: An in situ hybridization study. *J. Chem. Neuroanat.* **24**, 225–242 (2002).
16. C. Y. Yonamine *et al.*, Postmortem brains from subjects with diabetes mellitus display reduced GLUT4 expression and soma area in hippocampal neurons: Potential involvement of inflammation. *Cells* **12**, 1250 (2023).
17. B. Kula *et al.*, D-β-hydroxybutyrate stabilizes hippocampal CA3-CA1 circuit during acute insulin resistance. *PNAS Nexus* **3**, pgae196 (2024).
18. A. G. Chesebro, L. R. Mujica-Parodi, C. Weistuch, Ion gradient-driven bifurcations of a multi-scale neuronal model. *Chaos, Solitons Fractals* **167**, 113120 (2023).
19. S. Cunnane *et al.*, Brain fuel metabolism, aging, and Alzheimer's disease. *Nutrition* **27**, 3–20 (2011).
20. S. C. Cunnane *et al.*, Brain energy rescue: An emerging therapeutic concept for neurodegenerative disorders of ageing. *Nat. Rev. Drug Discovery* **19**, 609–633 (2020).
21. P. Puchalska, P. A. Crawford, Multi-dimensional roles of ketone bodies in fuel metabolism, signaling, and therapeutics. *Cell Metab.* **25**, 262–284 (2017).
22. E. Croteau *et al.*, A cross-sectional comparison of brain glucose and ketone metabolism in cognitively healthy older adults, mild cognitive impairment and early Alzheimer's disease. *Exp. Gerontol.* **107**, 18–26 (2018).
23. M. Fortier *et al.*, A ketogenic drink improves cognition in mild cognitive impairment: Results of a 6-month RCT. *Alzheimer's Dementia* **17**, 543–552 (2021).
24. A. J. Murray *et al.*, Novel ketone diet enhances physical and cognitive performance. *FASEB J.* **30**, 4021 (2016).
25. R. Krikorian *et al.*, Dietary ketosis enhances memory in mild cognitive impairment. *Neurobiol. Aging* **33**, 425.e19 (2012).
26. K. Sato *et al.*, Insulin, ketone bodies, and mitochondrial energy transduction. *FASEB J.* **9**, 651–658 (1995).
27. T. R. Matsuura, P. Puchalska, P. A. Crawford, D. P. Kelly, Ketones and the heart: Metabolic principles and therapeutic implications. *Circ. Res.* **132**, 882–898 (2023).
28. Y. Kashiwaya *et al.*, D-β-hydroxybutyrate protects neurons in models of Alzheimer's and Parkinson's disease. *Proc. Natl. Acad. Sci. U.S.A.* **97**, 5440–5444 (2000).
29. B. Biswal, F. Z. Yetkin, V. M. Haughton, J. S. Hyde, Functional connectivity in the motor cortex of resting human brain using echo-planar MRI. *Magn. Reson. Med.* **34**, 537–541 (1995).
30. C. F. Beckmann, M. DeLuca, J. T. Devlin, S. M. Smith, Investigations into resting-state connectivity using independent component analysis. *Philos. Trans. R. Soc. B: Biol. Sci.* **360**, 1001–1013 (2005).
31. E. Bullmore, O. Sporns, Complex brain networks: Graph theoretical analysis of structural and functional systems. *Nat. Rev. Neurosci.* **10**, 186–198 (2009).
32. B. T. T. Yeo *et al.*, The organization of the human cerebral cortex estimated by intrinsic functional connectivity. *J. Neurophysiol.* **106**, 1125–1165 (2011).
33. R. M. Hutchison *et al.*, Dynamic functional connectivity: Promise, issues, and interpretations. *NeuroImage* **80**, 360–378 (2013).
34. J. V. Haxby, "Multivariate pattern analysis of fMRI data: High-dimensional spaces for high-dimensional cognitive representations" in *Neuroimaging of Human Memory* (Oxford University Press, 2012), pp. 55–71.
35. A. Roebroeck, E. Formisano, R. Goebel, Mapping directed influence over the brain using Granger causality and fMRI. *NeuroImage* **25**, 230–242 (2005).
36. C. Preibisch, J. G. Castrillón, M. Bührer, V. Riedl, Functional MRI using sensitivity-encoded echo planar imaging (SENSE-EPI). *NeuroImage* **100**, 126–136 (2015).

37. A. M. Golestani, J. B. Kwinta, Y. B. Khatamian, J. J. Chen, The effect of temporal resolution on connectivity measures in resting state fMRI. *NeuroImage* **147**, 880–892 (2017).

38. Y. Tong, L. M. Hocke, S. C. Licata, B. D. Frederick, Evaluating the effects of resting period duration on functional connectivity in resting-state fMRI studies. *Front. Neurosci.* **13**, 1044 (2019).

39. L. Demetriou *et al.*, A comprehensive evaluation of increasing temporal resolution with multiband-accelerated protocols and effects on statistical outcome measures in fMRI. *NeuroImage* **176**, 404–416 (2018).

40. J. E. Chen, J. R. Polimeni, S. Bollmann, G. H. Glover, The impact of sampling rate on the detection of resting state functional connectivity in ultra high field fMRI. *NeuroImage* **152**, 292–305 (2017).

41. Z. Yu-Feng *et al.*, Altered baseline brain activity in children with ADHD revealed by resting-state functional MRI. *Brain Dev.* **29**, 83–91 (2007).

42. M. J. Hawrylycz *et al.*, An anatomically comprehensive atlas of the adult human brain transcriptome. *Nature* **489**, 391–399 (2012).

43. G. Gryglewski *et al.*, Spatial analysis and high resolution mapping of the human whole-brain transcriptome for integrative analysis in neuroimaging. *Neuroimage* **176**, 259–267 (2018).

44. A. Subramanian *et al.*, Gene set enrichment analysis: A knowledge-based approach for interpreting genome-wide expression profiles. *Proc. Natl. Acad. Sci. U.S.A.* **102**, 15545–15550 (2005).

45. E. H. Corder *et al.*, Gene dose of apolipoprotein e type 4 allele and the risk of Alzheimer's disease in late onset families. *Science* **261**, 921–923 (1993).

46. A. M. Saunders *et al.*, Association of apolipoprotein E allele e4 with late-onset familial and sporadic Alzheimer's disease. *Neurology* **43**, 1467 (1993).

47. D. M. Michaelson, Apoe ϵ4: The most prevalent yet understudied risk factor for Alzheimer's disease. *Alzheimer's Dementia* **10**, 861–868 (2014).

48. E. C. McNay, J. Pearson-Leary, GLUT4: A central player in hippocampal memory and brain insulin resistance. *Exp. Neurol.* **323**, 113076 (2020).

49. X. Shen *et al.*, Nonlinear dynamics of multi-omics profiles during human aging. *Nat. Aging* **4**, 1619–1634 (2024).

50. B. Lehallier *et al.*, Undulating changes in human plasma proteome profiles across the lifespan. *Nat. Med.* **25**, 1843–1850 (2019).

51. Y. Gazes *et al.*, Effects of brain maintenance and cognitive reserve on age-related decline in three cognitive abilities. *J. Gerontol.: Ser. B* **78**, 1284–1293 (2023).

52. F. Béland, M. V. Zunzunegui, B. Alvarado, A. Otero, T. Del Ser, Trajectories of cognitive decline and social relations. *J. Gerontol. Ser. B: Psychol. Sci. Soc. Sci.* **60**, P320–P330 (2005).

53. R. C. Petersen, Mild cognitive impairment. *N. Engl. J. Med.* **364**, 2227–2234 (2011).

54. T. A. Salthouse, When does age-related cognitive decline begin? *Neurobiol. Aging* **30**, 507–514 (2009).

55. J. Hardy, D. J. Selkoe, The amyloid hypothesis of Alzheimer's disease: Progress and problems on the road to therapeutics. *Science* **297**, 353–356 (2002).

56. M. Goedert, Alzheimer's and Parkinson's diseases: The prion concept in relation to assembled aβ, tau, and α-synuclein. *Science* **349**, 1255555 (2015).

57. M. T. Lin, M. F. Beal, Mitochondrial dysfunction and oxidative stress in neurodegenerative diseases. *Nature* **443**, 787–795 (2006).

58. J. T. Wang, Z. A. Medress, B. A. Barres, Axon degeneration: Molecular mechanisms of a self-destruction pathway. *J. Cell Biol.* **196**, 7–18 (2012).

59. A. Fischer, F. Sananbenesi, X. Wang, M. Dobbin, L. H. Tsai, Recovery of learning and memory is associated with chromatin remodelling. *Nature* **447**, 178–182 (2007).

60. S. J. Chinta *et al.*, Cellular senescence and the aging brain. *Exp. Gerontol.* **68**, 3–7 (2015).

61. C. López-Otín, M. A. Blasco, L. Partridge, M. Serrano, G. Kroemer, The hallmarks of aging. *Cell* **153**, 1194–1217 (2013).

62. M. D. Sweeney, K. Kisler, A. Montagne, A. W. Toga, B. V. Zlokovic, The role of brain vasculature in neurodegenerative disorders. *Nat. Neurosci.* **21**, 1318–1331 (2018).

63. C. Franceschi, P. Garagnani, P. Parini, C. Giuliani, A. Santoro, Inflammaging: A new immune-metabolic viewpoint for age-related diseases. *Nat Rev. Endocrinol.* **14**, 576–590 (2018).

64. D. A. Nation *et al.*, Blood-brain barrier breakdown is an early biomarker of human cognitive dysfunction. *Nat. Med.* **25**, 270–276 (2019).

65. J. Cohen, C. Torres, Astrocyte senescence: Evidence and significance. *Aging cell* **18**, e12937 (2019).

66. G. Ashrafi, Z. Wu, R. J. Farrell, T. A. Ryan, GLUT4 mobilization supports energetic demands of active synapses. *Neuron* **93**, 606–615 (2017).

67. M. Wilhelm *et al.*, Mass-spectrometry-based draft of the human proteome. *Nature* **509**, 582–587 (2014).

68. N. Fortelny, C. M. Overall, P. Pavlidis, G. V. C. Freue, Can we predict protein from mRNA levels? *Nature* **547**, E19–E20 (2017).

69. I. Khatir *et al.*, Decoupling of mRNA and protein expression in aging brains reveals the age-dependent adaptation of specific gene subsets. *Cells* **12**, 615 (2023).

70. M. Y. Donath, S. E. Shoelson, Type 2 diabetes as an inflammatory disease. *Nat. Rev. Immunol.* **11**, 98–107 (2011).

71. M. A. Creager, T. F. Lüscher, F. Cosentino, J. A. Beckman, Diabetes and vascular disease: Pathophysiology, clinical consequences, and medical therapy: Part I. *Circulation* **108**, 1527–1532 (2003).

72. R. B. Paisey, J. Harkness, M. Hartog, T. Chadwick, The effect of improvement in diabetic control on plasma and whole blood viscosity. *Diabetologia* **19**, 345–349 (1980).

73. H. van Nieuwenhuizen *et al.*, Ketosis elevates antioxidants and enhances neural function through improved bioenergetics: A ^{1}H MR spectroscopy study. bioRxiv [Preprint] (2024). https://doi.org/10.1101/2024.10.22.619722 (Accessed 10 October 2024).

74. Ja. Kim, Y. Wei, J. R. Sowers, Role of mitochondrial dysfunction in insulin resistance. *Circ. Res.* **102**, 401–414 (2008).

75. K. F. Petersen *et al.*, Mitochondrial dysfunction in the elderly: Possible role in insulin resistance. *Science* **300**, 1140–1142 (2003).

76. J. P. Ryan, D. F. Fine, C. Rosano, Type 2 diabetes and cognitive impairment: Contributions from neuroimaging. *J. Geriatr. Psychiatry Neurol.* **27**, 47–55 (2014).

77. R. M. Sapolsky, Glucocorticoid toxicity in the hippocampus: Reversal by supplementation with brain fuels. *J. Neurosci.* **6**, 2240–2244 (1986).

78. F. Alfaro-Almagro *et al.*, Image processing and quality control for the first 10,000 brain imaging datasets from UK biobank. *Neuroimage* **166**, 400–424 (2018).

79. S. Y. Bookheimer *et al.*, The lifespan human connectome project in aging: An overview. *Neuroimage* **185**, 335–348 (2019).

80. R. O. Roberts *et al.*, The mayo clinic study of aging: Design and sampling, participation, baseline measures and sample characteristics. *Neuroepidemiology* **30**, 58–69 (2008).

81. J. R. Taylor *et al.*, The Cambridge Centre for Ageing and Neuroscience (CAM-CAN) data repository: Structural and functional MRI, MEG, and cognitive data from a cross-sectional adult lifespan sample. *Neuroimage* **144**, 262–269 (2017).

82. R. Kumar *et al.*, Ground-truth "resting-state" signal provides data-driven estimation and correction for scanner distortion of fMRI time-series dynamics. *NeuroImage* **227**, 117584 (2021).

83. O. Esteban *et al.*, fMRIPrep: A robust preprocessing pipeline for functional MRI. *Nat. Methods* **16**, 111–116 (2019).

84. A. Abraham *et al.*, Machine learning for neuroimaging with scikit-learn. *Front. Neuroinf.* **8**, 14 (2014).

85. S. Wang *et al.*, Evaluation of field map and nonlinear registration methods for correction of susceptibility artifacts in diffusion MRI. *Front. Neuroinf.* **11**, 17 (2017).

86. N. Leonardi, D. Van De Ville, On spurious and real fluctuations of dynamic functional connectivity during rest. *Neuroimage* **104**, 430–436 (2015).

87. B. A. Seitzman *et al.*, A set of functionally-defined brain regions with improved representation of the subcortex and cerebellum. *Neuroimage* **206**, 116290 (2020).

88. P. Virtanen *et al.*, Scipy 1.0: Fundamental algorithms for scientific computing in Python. *Nat. Methods* **17**, 261–272 (2020).

89. S. Seabold *et al.*, "Econometric and statistical modeling with Python" in *Proceedings of the 9th Python in Science Conference* (Python for Scientific Computing Austin, TX, 2010), vol. 28.

90. M. H. Hagenauer *et al.*, Resource: A curated database of brain-related functional gene sets (Brain.GMT). *MethodsX* **13**, 102788 (2024).

91. E. T. Rolls, C. C. Huang, C. P. Lin, J. Feng, M. Joliot, Automated anatomical labelling atlas 3. *Neuroimage* **206**, 116189 (2020).

92. R. D. Markello *et al.*, Neuromaps: Structural and functional interpretation of brain maps. *Nat. Methods* **19**, 1472–1479 (2022).

93. B. B. Antal *et al.*, "Protecting the Aging Brain: fMRI study of the aging brain in acute ketosis", Openneuro. Available at https://openneuro.org/datasets/ds005405. Deposited 6 August 2024.

94. B. B. Antal, A. Amgalan, L. R. Mujica-Parodi, Analysis Scripts, GitHub. https://github.com/lcneuro/pub_pagb. Deposited 3 February 2025.